ADVANCED MATERIALS
www.advmat.de

Dopant Segregation Boosting High-Voltage Cyclability of Layered Cathode for Sodium Ion Batteries

Kuan Wang, Hui Wan, Pengfei Yan, Xiao Chen, Junjie Fu, Zhixiao Liu, Huiqiu Deng,* Fei Gao, and Manling Sui**

As a widely used approach to modify a material's bulk properties, doping can effectively improve electrochemical properties and structural stability of various cathodes for rechargeable batteries, which usually empirically favors a uniform distribution of dopants. It is reported that dopant aggregation effectively boosts the cyclability of a Mg-doped P2-type layered cathode ($Na_{0.67}Ni_{0.33}Mn_{0.67}O_2$). Experimental characterization and calculation consistently reveal that randomly distributed Mg dopants tend to segregate into the Na-layer during high-voltage cycling, leading to the formation of high-density precipitates. Intriguingly, such Mg-enriched precipitates, acting as 3D network pillars, can further enhance a material's mechanical strength, suppress cracking, and consequently benefit cyclability. This work not only deepens the understanding on dopant evolution but also offers a conceptually new approach by utilizing precipitation strengthening design to counter cracking related degradation and improve high-voltage cyclability of layered cathodes.

Layer structured alkali transition metal oxides are an important group of cathode materials for lithium ion batteries (LIBs),[1–3] sodium ion batteries (SIBs),[4–6] and potassium ion batteries (PIBs).[7,8] Either in the form of O3 structure, P2 structure or other else structures, their common similarity is the layer by layer stacking sequence of transition metal ions, oxygen ions, and alkaline ions.[9,10] Such a layered structure not only enables high-specific capacity but also favors the fast migration of alkaline ions due to the unique 2D diffusion pathway. Thus, layer structured $LiCoO_2$, ternary NMC ($LiNi_xMn_yCo_zO_2$, $x + y + z = 1$), and NCA ($LiNi_{0.85}Co_{0.1}Al_{0.05}O_2$) have achieved great commercial success as high-performance cathode materials for LIBs.[11–13] Other layered cathode materials, such as Ni-rich NMC for LIBs[14,15] and Na-NMC layered cathodes for SIBs, are gaining increasing attentions.[12,16,17]

One of the primary efforts on layered cathodes is further unlocking its capacity potential by narrowing the gap between the practical capacity and theoretical capacity. However, increasing the utilization of alkaline ions, usually by elevating the high-charge cutoff voltage, results in structural instability of the layered cathodes, due to aggravated surface/interface chemical degradations and bulk degradations.[18–20] The surface/interface degradations are attributed to the chemical reactions between cathode and electrolyte, which leads to cathode surface phase transition,[21,22] active material dissolution,[23] passivation layer formation,[24] electrolyte consumption,[25] and so on. For bulk degradations, irreversible bulk phase transition and cracking are the two main failure mechanisms. At high state of charge, phase transition not only destructs the active layered structure but also introduces substantial volume changes causing mechanical failures. A direct correlation between phase transition and cracking has been established in the P2 layered cathode for SIBs.[26] Cleavage along layered planes leads to the typical intragranular cracking for many layered cathodes, which has been frequently observed after high-voltage cycling.[26–28] The detrimental effects of cracking include fracture caused disintegration,[28] which leads to poor electronic conduction[29,30] and loss of active materials, and new surfaces exposure to electrolyte which results in cathode surface degradation[31–33] and electrolyte consumption. In addition, high density of intragranular cracks also plagues battery thermal stability and safety.[27]

Doping electrochemically inactive elements has been verified as an effective method to improve the electrochemical performance of layered cathodes.[34,35] Dopants can play multiroles in engineering bulk material, such as eliminating unwanted

K. Wang, Prof. P. Yan, J. Fu, Prof. M. Sui
Beijing Key Laboratory of Microstructure and Properties of Solids
Institute of Microstructure and Properties of Advanced Materials
Beijing University of Technology
Beijing 100124, China
E-mail: pfyan@bjut.edu.cn; mlsui@bjut.edu.cn
H. Wan, Prof. Z. Liu, Prof. F. Gao
College of Materials Science and Engineering
Hunan University
Changsha 410082, China
Dr. X. Chen
Beijing Key Laboratory of Green Chemical Reaction Engineering and Technology
Department of Chemical Engineering
Tsinghua University
Beijing 100084, P. R. China
Prof. H. Deng
School of Physics and Electronics
Hunan University
Changsha 410082, China
E-mail: hqdeng@hnu.edu.cn
Prof. F. Gao
Department of Nuclear Engineering and Radiological Sciences
University of Michigan
Ann Arbor, MI 48109, USA
The ORCID identification number(s) for the author(s) of this article can be found under https://doi.org/10.1002/adma.201904816.

DOI: 10.1002/adma.201904816

order–disorder transition,[34,36] suppressing lattice structure transition,[36,37] tuning the spacing of layered planes,[38] acting as pillars to strengthen mechanical properties.[39,40] Thus, fully and in-depth understanding the role of each specific dopant is in urgent need, especially their atomistic mechanism. In this work, we select a typical layered cathode, Mg-doped P2-structured $Na_{0.67}Ni_{0.33-x}Mn_{0.67}Mg_xO_2$ (NMM), to investigate how Mg dopant improves the cyclability using advanced electron microscopy and density functional theory (DFT) calculations. We reveal that Mg-dopants can effectively suppress the intragranular cracking and maintain bulk materials integration during high-voltage cycling, which well elucidates the improved cycling performance of Mg-doped NMM samples. Surprisingly, our observations verify that Mg dopants can migrate and segregate as precipitates in grain bulk during high-voltage cycling. Such a dopant evolution, from uniformly distributed state to nanosized precipitates during cycling, can effectively suppress intragranular crack and improve cycling stability, which suggests a new strategy to counter mechanical disintegration of layered cathodes by a precipitation strengthening mechanism. This work also reveals the substantial ion migration phenomenon during high-voltage cycling is a critical challenge for high-voltage usage of layered cathodes.

Pristine P2-$Na_{0.67}Ni_{0.33}Mn_{0.67}O_2$ (P2-NM) and Mg-doped P2-$Na_{0.67}Ni_{0.33-x}Mn_{0.67}Mg_xO_2$ (P2-NMM, $x = 0.05$ or 0.1) cathode materials are synthesized by solid state method, whose structure and composition are verified by X-ray diffraction (XRD) and energy dispersive X-ray spectroscopy (EDS) analysis (Figure S1, Tables S1–S3, and Figure S2, Supporting Information). Their electrochemical performance is tested in half-cells with Na metal as the counter electrode. The cycling voltage window is 2.0–4.5 V with the rate of 0.1 C (17.3 mA g^{-1}). All P2-NM cells suffer significant capacity decay, while the Mg-doped P2-$Na_{0.67}Ni_{0.28}Mn_{0.67}Mg_{0.05}O_2$ (P2-NMM05) and P2-$Na_{0.67}Ni_{0.23}Mn_{0.67}Mg_{0.1}O_2$ (P2-NMM10) cells show much improved capacity retentions. **Figure 1**a

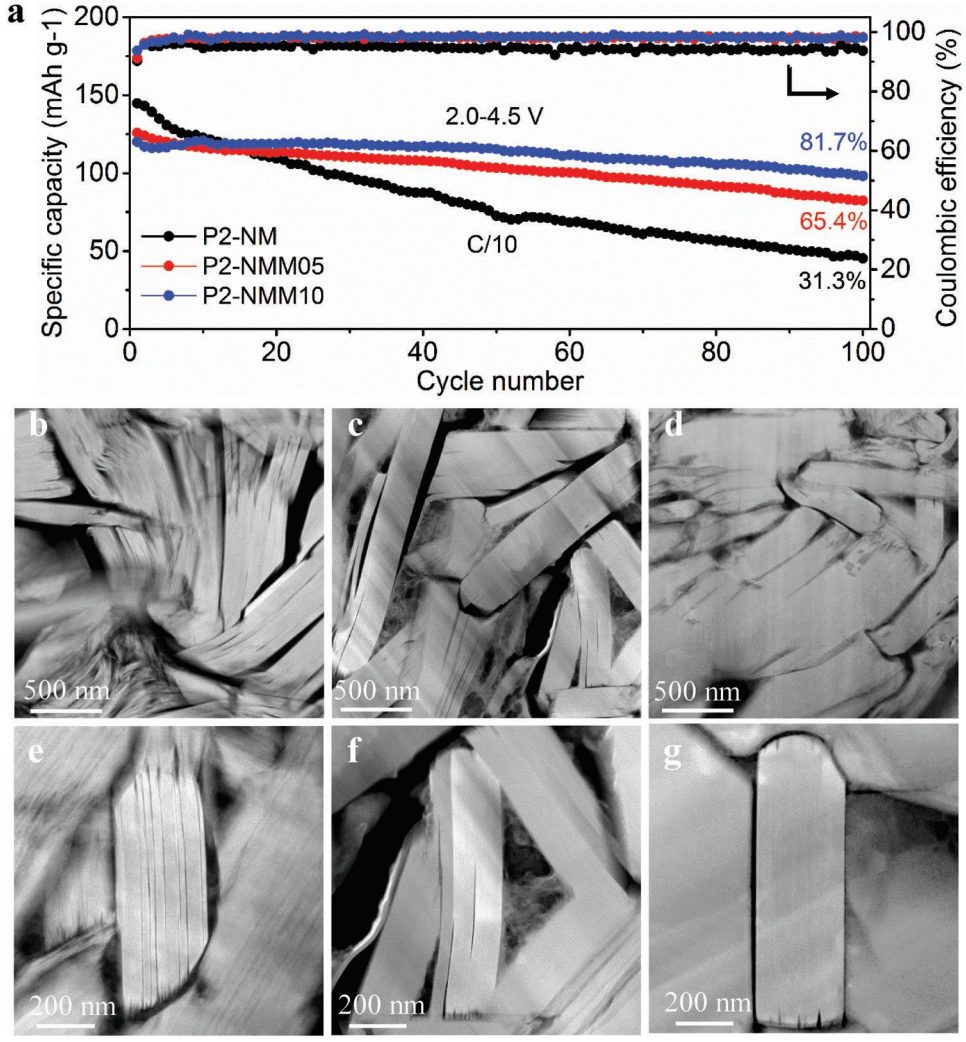

Figure 1. Mg-doping improving cycling stability and material integrity. Electrochemical performance and cross-sectional STEM-HAADF images of the three P2-structured cathode materials, P2-NM, P2-NMM05, and P2-NMM10. a) Capacity retentions and coulombic efficiencies as a function of cycle numbers. b–g) Cross-sectional STEM-HAADF images of the three cathode materials after 50 cycles at 2.0–4.5 V. (b) Material disintegration is severe in the cycled P2-NM cathode. Fewer cracks are observed in (c) the cycled P2-NMM05 cathode and (d) the cycled P2-NMM10 cathode. e) High density of intragranular cracks are observed in the cycled P2-NM cathode. f) Low density of intragranular cracks in the cycled P2-NMM05 cathode. g) Cracks are short and mainly located at particle surface region in the cycled P2-NMM10 cathode.

represents the capacity retentions and corresponding coulombic efficiencies of the three electrode materials. After 100 cycles, the capacity retention is 31.3% for the undoped P2-NM, while the P2-NMM05 and the P2-NMM10 are 65.4% and 81.7%, respectively. Increasing the Mg dopant concentration from 5% to 10% though decreases the initial discharge capacity slightly, the cycle stability is enhanced substantially. The enhanced electrochemical performance of 200 cycles is shown in Figure S3 of the Supporting Information. Voltage fading issue is also alleviated for the Mg-doped P2-NMM cells, which is verified by the charge–discharge voltage profiles and their corresponding dQ/dV curves as shown in Figure S4 of the Supporting Information. The above electrochemical results validate that Mg doping is an effective method to stabilize the high-voltage cycling performance of the P2-NM layered cathode. Performance improvements usually originate from the improved structure stability. Previous studies have shown that Mg doping can lead to the P2-OP4 phase transition with much smaller volume changes in comparison with the P2-O2 phase transition in the undoped material,[36,41] which is also confirmed by our XRD measurement (Figure S5, Supporting Information). Furthermore, our structural analysis reveals that cracking resulted grain disintegration has been effectively suppressed via Mg-doping as shown in Figure 1b–g. Cross-sectional low magnification scanning transmission electron microscopy-high angle annular dark field (STEM-HAADF) images (Figure 1b–d) show that high density of cracks are formed in the P2-NM cathode after 50 cycles, while cracks in the cycled P2-NMM05 and P2-NMM10 are much less. At higher magnification Figure 1e–g, we can see the cracks run through the whole grain in the undoped P2-NM cathode, while the density and length of cracks decrease significantly in the cycled P2-NMM05 sample. For the cycled P2-NMM10 sample, the interior cracks are bare, only some cracks appear at the particle surface. Cross-sectional scanning electron microscopy (SEM) observations show consistent results that the density of crack decreases significantly in the Mg-doped P2-NMM samples (Figure S6, Supporting Information). Large volume change induced high internal strain is one of the major causes for cracking. Mg doping can change the original P2-O2 phase transition into P2-OP4 phase transition at high desodiation, which minimizes volume changes and thus effectively suppresses the crack formation.

One may argue that the fast performance decay of the undoped P2-NM is due to its deeper desodiation at the first few cycles. As shown in Figure 1a, the capacity is higher for the undoped P2-NM during the first several cycles. To eliminate such a concern, we cycled the undoped P2-NM electrode at lower specific capacity by lowering the high-charge cutoff voltage to 4.2 V. As shown in Figure S7a of the Supporting Information, the undoped P2-NM cathode still suffers much faster capacity decay than the Mg-doped P2-NMM cathode, even though their initial discharge capacities are almost the same. Cross-sectional SEM and HAADF images verified high density of intragranular cracks in the P2-NM cathode after 50 cycles at 4.2 V (Figure S7b,c, Supporting Information). Thus, Mg-doping can effectively mitigate grain cracking, leading to improved cycling stability.

For the as-synthesized Mg-doped samples, dopant distribution in grain bulk is uniform as revealed by the STEM-EDS mapping (Figure S2, Supporting Information). **Figure 2**a,d from the uncycled P2-NMM05 sample and P2-NMM10 sample show clean and uniform contrast in grain bulk before cycling. Unexpectedly, Mg elemental dopants are tended to segregate into nanoprecipitates during high-voltage cycling, which has been verified in the Mg-doped P2-NMM05 and P2-NMM10 samples. For the P2-NMM05 sample, though no appreciable change is observed after 10 cycles (Figure 2b), after 50 cycles, some bright stripes are developed in grain bulk (highlighted by red arrows in Figure 2c). For the P2-NMM10 sample, bright stripes are developed much easier. As shown in Figure 2e,f, high density of bright stripes are developed after 10 cycles and their density and size increase significantly after 50 cycles (more examples are shown in Figure S8, Supporting Information). Figure 2g is an STEM-EDS mapping from the P2-NMM10 sample after 50 cycles, in which it shows the bright stripes are Na-deficient and Mg-rich regions, appeared as precipitates. (More examples are shown in Figures S9 and S10, Supporting Information.) The EDS mappings also reveal that the concentrations of transition metal elements, Ni and Mn, do not have appreciable fluctuation between the precipitates and the matrix, indicating the formation of precipitate is mainly due to the rearrangement of Na and Mg.

Atomic resolution EDS mapping is also conducted on the pristine and cycled samples. Before cycling, Mg distribution is uniform as shown in Figure S11 of the Supporting Information. After cycling, as shown in **Figure 3**a and Figure S10 (Supporting Information), at the center of each bright stripe, we can observe the clear composition change, where Na is depleted and Mg is enriched, while Ni and Mn still remain their original layered structure both in the matrix and the precipitates. Therefore, Mg dopants are segregated at the Na-layers rather than the TM layers. Composition change leads to the lattice structure transition. Figure 3b–d shows the lattice images of the precipitates. The highlighted yellow regions are not in P2 lattice structure, which adopts a different stacking sequence as indicated by the yellow lines. Due to the lattice structure change, the layered plane spacing is also reduced. As shown in Figure 3b, the plane spacing is 5.0 Å, smaller than 5.6 Å of the P2 layered structure. The thickness of precipitate lamellas is pretty thin, ranging from single layer to several layers. Figure 3b–d and Figure S12 (Supporting Information) show the precipitates with different thickness. Figure 3d shows one end of a precipitate, in which the left side presents a perfect P2-layered structure and the right side shows an embedded precipitate. The yellow circuit highlights the lattice change from the matrix (left) to the precipitate (right), which indicates that the precipitate is formed by a shuffle mechanism.[42,43] For the multilayer precipitates (Figure 3c,d; Figure S12, Supporting Information), neighbored TM layers shuffle in opposite directions to minimize the geometrical strain between precipitate and matrix, as the red arrows illustrated in Figure 3e. For the cycled P2-NMM05 sample, we observed the similar composition and structural changes (Figures S12 and S13, Supporting Information). However, the precipitates can hardly be detected by diffraction techniques, such as XRD (Figure S14, Supporting Information) and electron diffraction (Figure S15, Supporting Information).

Elevating charge cutoff voltage usually leads to poor cycling stability. However, intriguingly, we find that the Mg-doped P2-NNM10 electrodes show better cycling stability when cycled

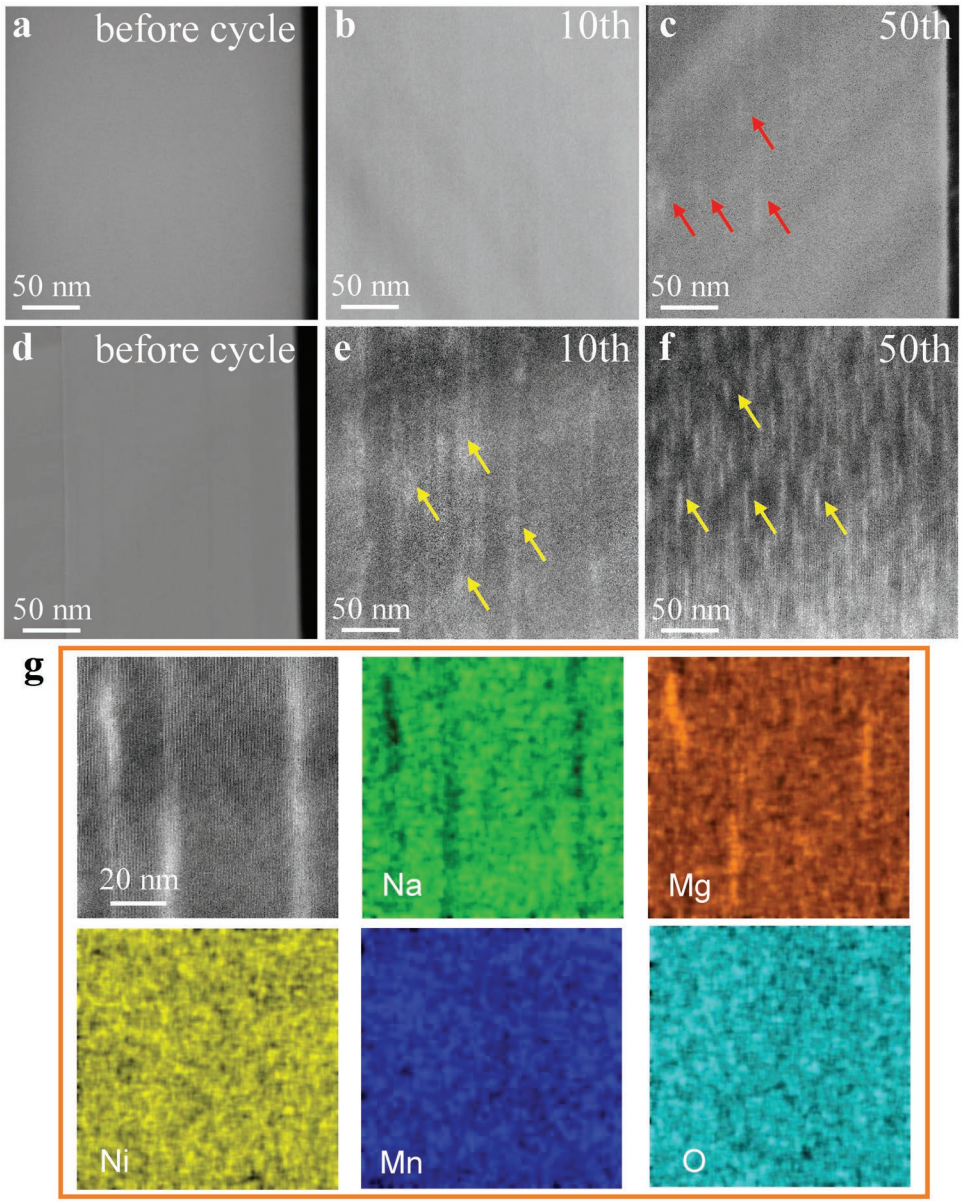

Figure 2. Electrochemical cycling inducing dopant segregation. STEM-HAADF images of the a–c) P2-NMM05 and d–f) P2-NMM10 cathode cycled at 2.0–4.5 V. (a) Typical image from the P2-NMM05 cathode before cycle, showing a uniform contrast in grain bulk. (b) No bright stripes in the P2-NMM05 cathode after 10 cycles. (c) Some bright stripes (red arrows) in the P2-NMM05 cathode after 50 cycles. d) Uniform contrast in grain bulk of the P2-NMM10 cathode before cycle. e) Low density of bright stripes (yellow arrows) in the P2-NMM10 cathode after 10 cycles. f) High density of bright stripes (yellow arrows) in the P2-NMM10 cathode after 50 cycles. g) STEM-HAADF image and corresponding EDS mapping, showing bright stripes are Mg-rich and Na-deficient regions. Ni, Mn, and O show no appreciable composition fluctuation.

at higher charge cutoff voltage. As shown in **Figure 4**a, when cycled at 2.0–4.5 V, the P2-NMM10 shows 82% capacity retention after 100 cycles. By contrast, when cycled at 2.0–4.3 V, the P2-NNM10 shows only 67% capacity retention after 100 cycles. Detailed structure analysis reveals that the cathode cycled at 2.0–4.3 V shows more cracks than the one cycled at 2.0–4.5 V. Figure 4b–d represents the P2-NMM10 cathode after 100 cycles at 4.3 V, in which high density of cracks are developed. Figure 4c shows that cracks are generated both from grain interior (blue arrows) and grain surface region (red arrows). (More observations are shown in Figure S16a–d , Supporting Information.) By contrast, for the sample cycled at 4.5 V, only the surface region generates small cracks and the well preserved bulk integrity is responsible for the better cycle stability. By scrutinizing the grains cycled at 4.3 and 4.5 V, we find the main difference of grain bulk is that there is bare precipitate in the sample cycled at 4.3 V (Figure 4d; Figure S16a–d, Supporting Information) but there are many precipitates in the sample cycled at 4.5 V (Figure S16f,h, Supporting Information). Furthermore, if a grain cycled at 4.5 V has no precipitate, it also has high density of cracks. A typical example is shown in Figure 4e, in which the grain highlighted by a blue frame has no precipitate but many cracks (Figure 4f),

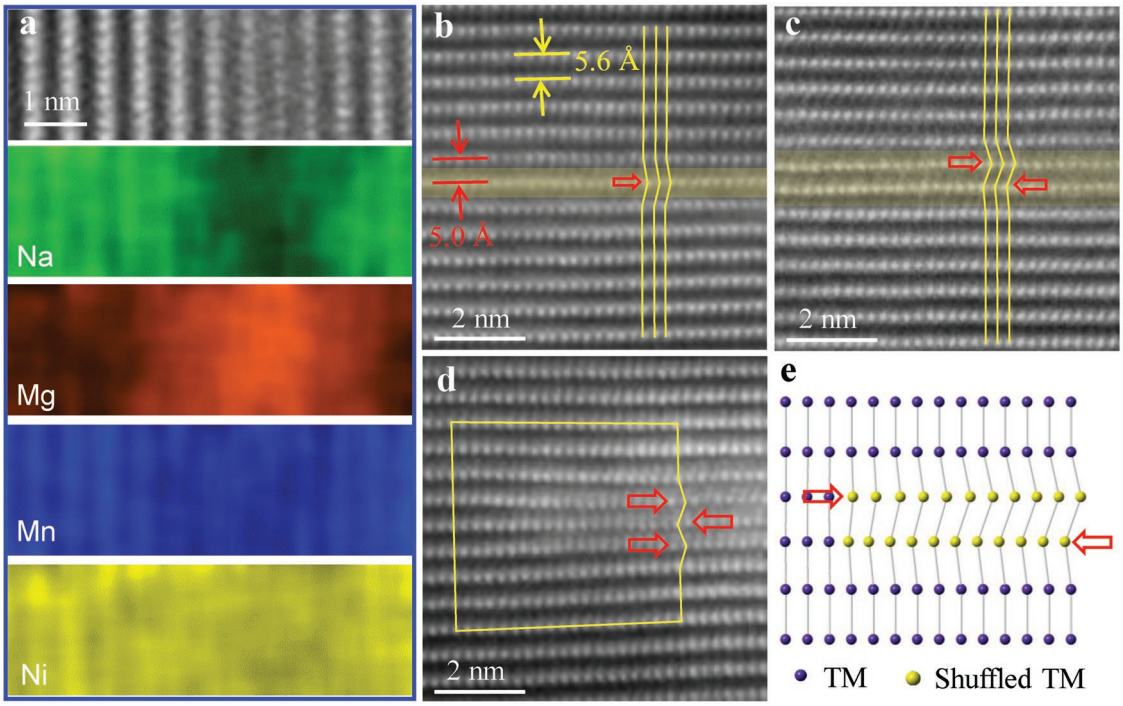

Figure 3. Elemental reorganization induced precipitates. a) Atomic resolution EDS mapping of the P2-NMM10 cathode after 50 cycles at 2.0–4.5 V, showing the distribution of Na, Mg, Mn, and Ni. (b–d) High resolution STEM-HAADF images. b) A single layer thick precipitate. c) A two-layer thick precipitate. Yellow regions highlight the phase transition layers whose stacking sequence is different from the P2 structure as indicated by the yellow lines. d) A multilayer precipitate with one end terminated in the P2 structured matrix. The yellow circuit highlights a zigzag stacking sequence due to displacement along the red arrows. e) Atomic model to show the formation of a two-layer precipitate, yellow balls represent the TM cations shuffled along red arrows.

while the grain highlighted by a red frame has many precipitates but few cracks (Figure 4g). Clearly, bulk structure with or without precipitates leads to different resistance to cracking. Thus, dopant segregation induced precipitates can more effectively suppress cracking. Figure 4f,g further confirms that the formation of precipitate is closely related to the cycling condition of each grain, together with the results shown in Figure 4d,g, indicating that adjusting cycling condition or recipe can be used to control the precipitate formation. For the P2-NMM05 sample, the capacity retention is 65.4% after 100 cycles at 2.0–4.5 V, which is also higher than the capacity retention 56.7% after 100 cycles at 2.0–4.3 V (Figure S17, Supporting Information). In a short summary, dopant segregation induced precipitations can more effectively suppress cracking as compared with the uniformly doping, which is the reason why the electrode cycled at 4.5 V shows better cycle stability than the one cycled at 4.3 V.

Above characterizations and analysis reveal that Mg segregation can enhance cycling stability due to the "precipitation strengthening" mechanism. To facilitate the dopant segregation, Mg ion migration is required during cycling. We performed DFT calculations to estimate the migration energy barrier of Mg ions. The calculation is based on the P2 structured $Na_{0.67}Ni_{0.23}Mn_{0.67}Mg_{0.1}O_2$ with different state of charge (SOC) (details of the calculations are described in the Experimental Section). For the uncycled Mg-doped material, DFT calculations show the formation energy to be 0.074 eV when Mg resides at TM layer, while the formation energy is 0.303 eV when Mg resides at Na layer. Therefore, Mg dopant is energetically favored to be positioned at TM layer rather than Na layer, which is consistent with previous reports.[34,36] To realize the observed Mg-enriched precipitates, two kinds of migration are required for Mg dopants. One is the cross-layer migration, by which Mg ions jump into Na layers from TM layers or vice versa. The other is the in-plane migration, by which Mg ions aggregate within the Na layers as verified by our aforementioned EDS analysis. The energy barrier of the cross-layer migration and the in-plane (Na layer) migration are calculated under different SOCs. **Figure 5**a shows the cross-layer migration results, in which the energy barrier is lower at high SOC, 0.8 eV for $Na_{0.08}Ni_{0.23}Mn_{0.67}Mg_{0.1}O_2$ and 1.8 eV for $Na_{0.46}Ni_{0.23}Mn_{0.67}Mg_{0.1}O_2$. Therefore, high SOC can reduce the energy barrier for Mg migration from the TM layer into the Na layer, which is consistent with our experimental observations that Mg-enriched precipitates are easily formed when cycled at 4.5 V. For the in-plane migration, high SOC leads to smaller plane spacing, which will increase the energy barrier for Mg migration,[44] as shown in Figure 5b. Overall, the in-plane migration is much easier than the cross-layer migration. As confirmed by our calculations that in-plane Mg-dopant aggregation is an energetically favored process. As shown in Figure 5c, the total energy can reduce 0.61 eV when two Mg dopants migrate together to form a paired Mg–Mg dimer. Therefore, DFT calculations verify that at high SOC Mg dopants are kinetically easier to migrate and energetically favor to aggregate, which explains the precipitation formation process suggested by experiments.

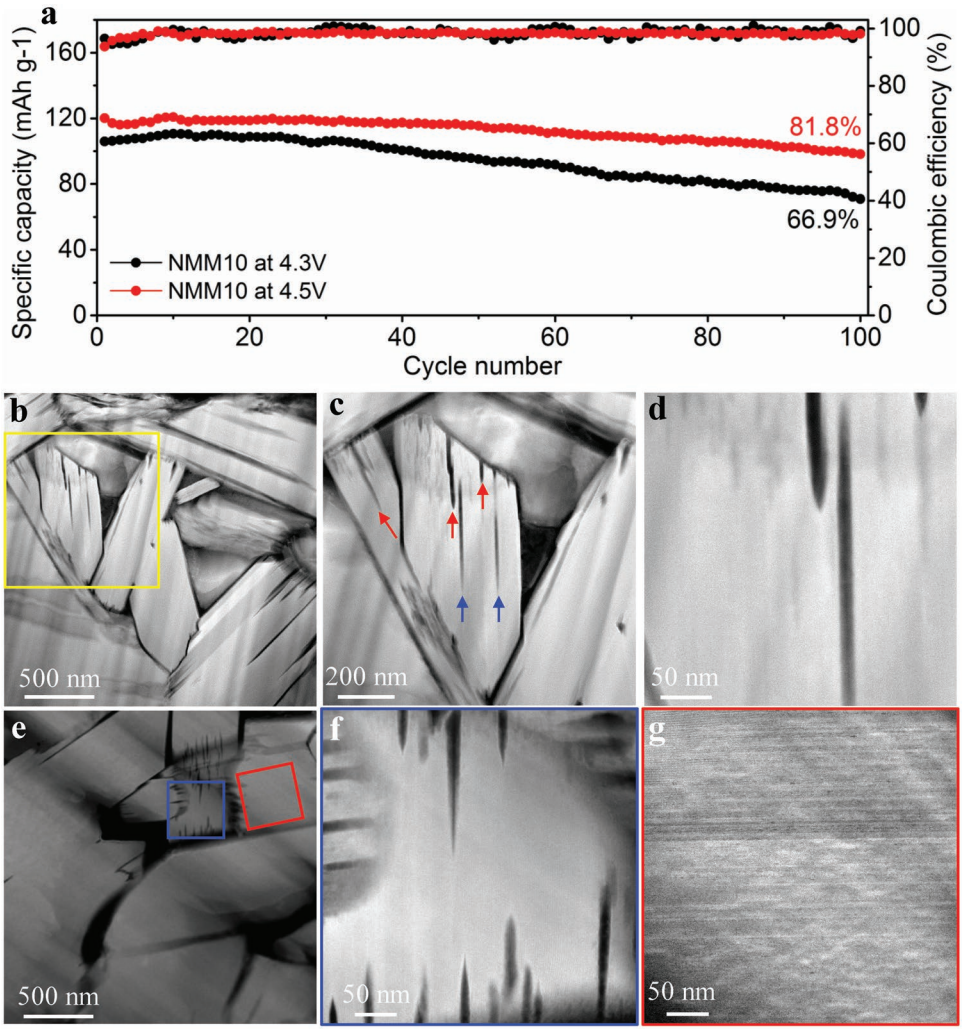

Figure 4. Dopant segregation benefiting cycle stability. Electrochemical performance and corresponding cross-sectional STEM-HAADF images of the P2-NMM10 cathode after 100 cycles. a) Capacity retentions and coulombic efficiencies as a function of cycle numbers. b) Higher density of cracks in P2-NMM10 sample cycled at 4.3 V. c) From the yellow frame in (b). Blue and red arrows highlight the cracks located at the grain interior and surface, respectively. d) No precipitate is observed in the particle. e) Cross-sectional HAADF image of P2-NMM10 cycled at 4.5 V. f) A particle without precipitates and many cracks. g) A neighbored particle with high density of precipitates and no crack.

In the as-synthesized Mg doped sample, Mg dopants are uniformly distributed in the bulk material, which leads to much improved cycling stability. As shown in **Figure 6**a, after 100 cycles at 2.0–4.3 V, the P2-NMM10 demonstrates 66.9% capacity retention, while the undoped P2-NM only has 31.3% capacity retention. When cycled at 2.0–4.3 V, the dopant distribution is still uniform and no precipitate has been observed (Figure 4b–d). Increasing the high-cutoff voltage to 4.5 V, dopant evolution induced Mg-enriched precipitates can be developed. Our aforementioned electrochemical tests and microstructure analysis indicate precipitates can further enhance cyclability. To further validate this conclusion, we first cycle the P2-NMM10 sample at 2.0–4.5 V for 10 cycles to introduce certain amount of precipitates and then lower the high-cutoff voltage to 4.3 V. As shown in Figure 6a, the capacity retention is further increased to 71.6% after 100 cycles. Therefore, it is more effective to stabilize the P2-NMM layered cathode when the uniform distributed dopants segregate into precipitates.

Inspired by our discovery of the precipitation formation phenomena and its precipitation strengthening mechanism, we propose that the precipitation strengthening mechanism can be a new strategy to enhance the cycling stability of layered cathodes to suppress cracking. As shown in Figure 6b, for the undoped layered cathode material, electrochemical cycling can introduce high density of cracks at both surface region and bulk. It is because the weak interlayer bonding at high desodiation makes cracking easily nucleate and propagate. For the doped layered cathode materials, as shown in Figure 6c, the uniformly distributed dopants can act as pillars to enhance the cycling stability, but the single atom pillars are relatively weak bonding, thus cracks can still be developed in grain bulk. For the precipitation strengthening mechanism, as shown in Figure 6d, dopants are segregated into precipitates in the grain bulk, which not only brings more dopants into the alkaline layers but also develops high density of precipitate pillars. The 3D network precipitates acting as strong pillars can

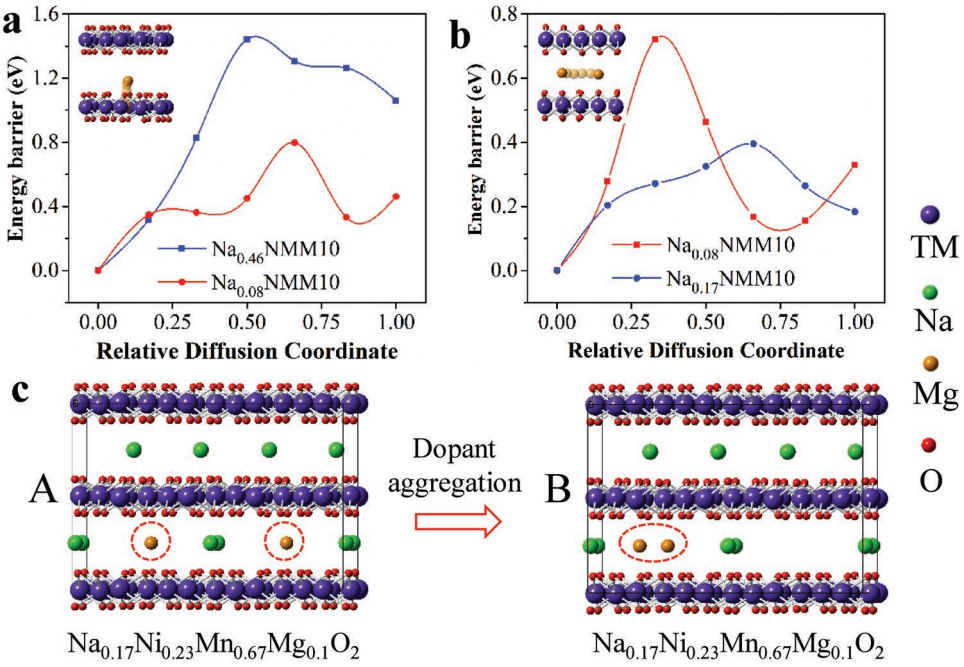

Figure 5. Calculation of Mg diffusion barrier and Mg–Mg formation energy. a) Cross-layer diffusion barrier for Mg from TM layer to Na layer in two states of charge (SOC). Inset shows the Mg migration pathway from TM layer into Na layer. b) In-plane diffusion barrier for Mg in two SOC. Inset shows the Mg migration pathway within the Na layer. c) Calculation of the formation energy changes as two Mg dopants (left) aggregate into a paired Mg–Mg dimer (right) within the Na layer. The total energy is reduced 0.61 eV after forming a Mg–Mg dimer.

greatly strengthen the bonding between TM layers to counter the internal strain and effectively suppress crack nucleation and propagation. The reason why doping can suppress cracking to achieve better cycle stability lies in two. One is the well-known phase stabilizing effect, by which the doping can change the P2-O2 phase transition into the P2-OP4 phase transition, minimizing strain buildup. The other one is the pillar effect, by which the mechanical strength of the layered cathode can be enhanced significantly, suppressing cracking formation.

Though dopant evolution induced precipitates can suppress cracking, it also can bring negative effects when dopant migration is severe. For instance, Mg segregation into the Na layers leads to a declined rate capability. As shown in Figure S18 of the Supporting Information, due to the blocking effect of dopant segregation, the rate capability of the P2-NMM10 is decreased, especially at high rates. In addition, after prolonged cycles, not only the bright stripes but also many dark spots are developed. As shown in Figure S19 of the Supporting Information, the density of dark spots are very high after 100 cycles. Our extensive observations indicate that high-cycling voltage, long cycle time, and dopant segregation are the three essential requirements to form the dark spots. These dark spots are presumably nanovoids as being revealed in the Li-rich layered cathodes.[45] Formation of high density of dopant precipitates and nanovoids indicates substantial mass transportation during high-voltage cycling, which can be a serious issue for high-voltage usage of this kind of cathode materials.

Based on microstructural characterizations and DFT calculations, we reveal that the improved cycling stability of Mg-doped P2-NMM layered cathode is mainly due to suppression of cracking. More importantly, we discover that the Mg dopants are tended to segregate in Na layers to form thin lamella-shaped precipitates upon high-voltage cycling. Intriguingly, the in situ formed precipitates can further strengthen the layered cathode and suppress cracking, which leads to the superior cycling stability at elevated voltage. Therefore, a new conceptual strategy by using "precipitation strengthening" is proposed, by which it is promising to further engineer the bulk material of various layered cathodes, either in the material synthesis process and/or during the cycling process, to alleviate mechanical disintegration and enhance cycling stability.

Experimental Section

Materials: $Na_{0.67}Ni_{0.33-x}Mn_{0.67}Mg_xO_2$ (x = 0, 0.05, 0.1) was synthesized via a solid state reaction method from stoichiometric values of Na_2CO_3, NiO, MgO, and Mn_2O_3. The mixtures were ground in an agate mortar and pressed into pellets with the diameter of 18 mm under a load of 14 MPa before calcining. The precursors were calcined at 900 °C in air for 16 h, then slowly cooling to room temperature and stored in an argon-filled glove box until use.

Electrochemical Measurements: Coin cells (CR2032) were assembled to evaluate the electrode performance of $Na_{0.67}Ni_{0.33-x}Mn_{0.67}Mg_xO_2$ (x = 0, 0.05, 0.1) of the fabricated electrodes in an argon-filled glove box (H_2O, O_2 < 0.1 ppm). Positive electrodes were prepared by mixing the active materials, acetylene black, and polyvinylidene fluoride binder at a mass ratio of 80:10:10 on Al foil, and then dried overnight at 80 °C in vacuum. Sodium foil and porous glass fiber were used as the counterelectrode and separator, respectively. Electrolyte solution was 1.0 M $NaClO_4$ dissolved in propylene carbonate with 5 vol% of fluoroethylene carbonate.

Characterization: Structural analysis of the samples was performed with the X-ray diffraction system (Bruker D8 Advance) using Cu Kα radiation (λ = 1.5418 Å). Rietveld refinement was performed using the RITAN-FP[46] program to obtain crystal structure parameters. The

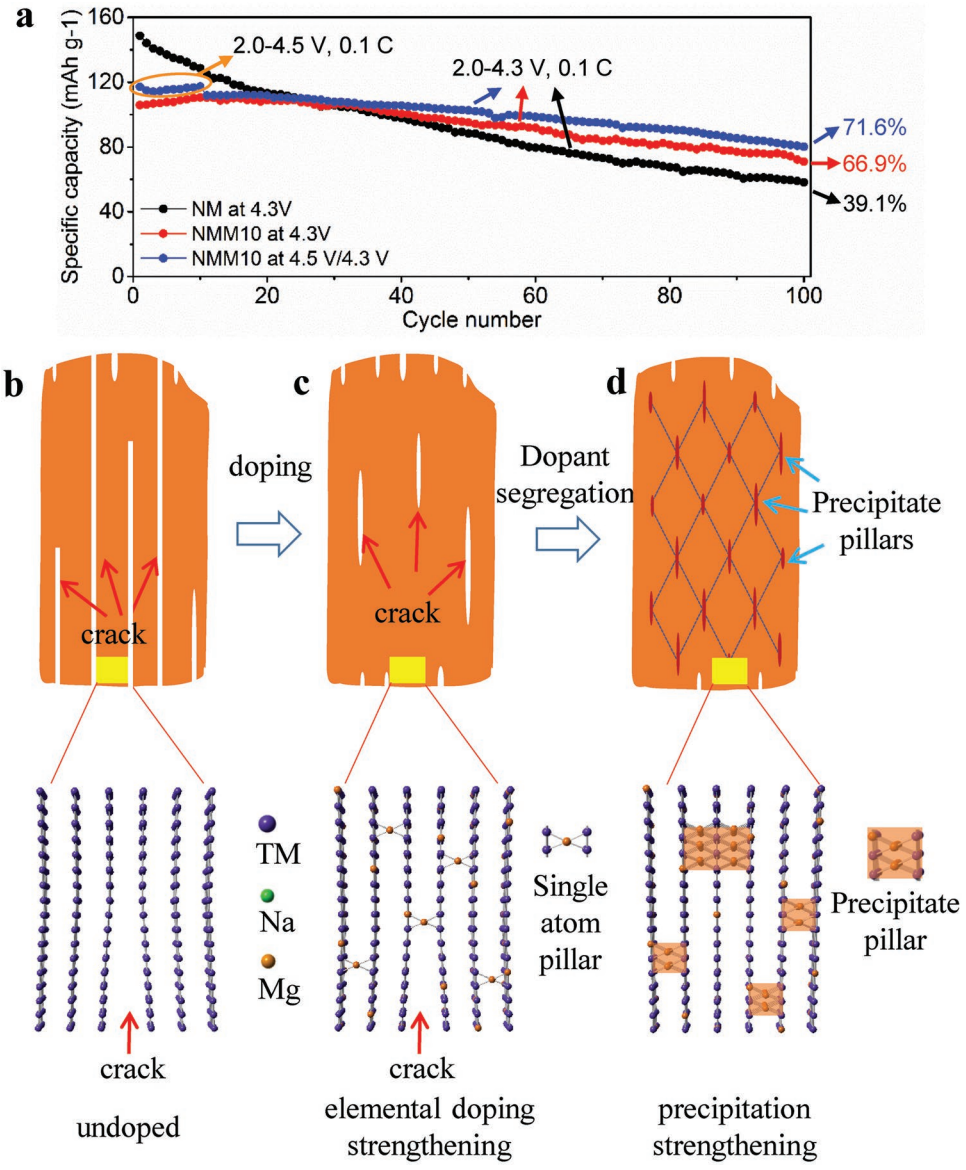

Figure 6. Precipitation strengthening mechanism to enhance cyclability. a) Capacity retentions as a function of cycle numbers. For the undoped P2-NM sample, capacity decay is fast as shown by the black dots. For the Mg-doped P2-NMM10 sample, introducing precipitates by cycling at 4.5 V for 10 cycles can achieve better cyclability than the one cycled only at 4.3 V (no precipitate). b) For undoped layered cathode, high-voltage cycling always incurs serious cracking issue due to the cleavage of layered planes. c) For a conventional doped sample, dopants are uniformly distributed within the bulk lattice. Only some dopants residing at the alkaline layers can act as pillars to mitigate cracking. Such single atom pillars are relative weak bonds, thus cracks can still be developed. d) By forming high density of nanoprecipitates, the 3D network structure can effectively suppress bulk cracking through the precipitation strengthening mechanism, which is a new strategy to maintain material integrity and improve cyclability.

TEM specimens were prepared using a focused ion beam (FEI Helios NanoLab 600i) operating at 2–30 kV. The prepared method can be found in the literature.[28] Samples were investigated by using an FEI Titan G2 60–300 microscope at 300 kV. This microscope is equipped with a probe spherical aberration corrector, enabling sub-angstrom imaging using STEM-HAADF detectors. For STEM-HAADF imaging, the inner and outer collection angles of an annular dark-field detector were 58.5 and 200 mrad, respectively. EDS analysis was performed using the high efficient "Super X" four-detector EDS detector by scanning the same region with multiple times with dwell time as 0.1 ms. The EDS data were collected and processed by using Esprit 1.9.

DFT Calculations: DFT[47] calculations with the projector augmented-wave[48] method were performed with the Vienna ab initio simulation package.[49] The Perdew–Burke–Ernzerhof functional was used for describing the electron–electron exchange-correlation, which is a generalized gradient approximation method.[48] In this calculation, the energy cutoff for the plane-wave basis set was set to 500 eV. The convergence criterion for structure optimization was 0.02 eV Å^{-1}. Undoped P2-NM was modeled by a $4 \times 4 \times 1$ supercell containing 16 Na sites, 16 Ni sites, 16 Mn sites, and 48 O sites. When one or more Ni atoms in the layer of the Ni–O octahedral structure were replaced by Mg atoms, it forms a $Na_{16}Ni_{16-x}Mg_xMn_{16}O_{48}$ supercell. In the undoped structure, both ions and lattices were relaxed. For the defect and diffusion structures, only the ion positions were allowed to relax while the lattice parameters are fixed. As the effect of spin configurations on the formation energies can be neglected, the ferromagnetic configuration was only considered.[50]

The diffusion energy barrier of Mg from one site to its neighbor one using climbing image nudged elastic band (CI-NEB) method was explored.[51] First, the initial and the final state were relaxed to achieve the minimum energy configurations. To search the transition state, five images were linearly generated between the fixed initial and final states. The energy difference between the initial state and the saddle image was defined as the diffusion barrier.

The formation energy for the Mg-doped material, both resides at TM layer and Na layer, was calculated based on the following equation

$$E_f = E_{Mg@M} - E_{perfect} - \mu_{Mg} + \mu_M \quad (1)$$

Here M is Ni or Na atom, $E_{Mg@M}$ is the total energy of Mg resides at TM layer or Na layer, $E_{perfect}$ represents the total energy of P2-NM. The μ_{Mg} and μ_M are chemical potential of the Mg and M atoms, respectively. The formation energy for two Mg dopants are estimated when they migrate together to form a Mg–Mg pair as shown in Figure 5c. In the process of modeling, the supercell of $4 \times 4 \times 1$ to $4 \times 8 \times 1$ is expanded, and then two Mg atoms are added as far as possible to the Na plane (model A) and two Mg atoms are put close together to form a Mg–Mg dimer (model B), the following equation was applied

$$E_f = E_B - E_A \quad (2)$$

where E_B and E_A are the total energy of model B and model A, respectively. The negative value of E_f represents an exothermic reaction, and a more negative value manifests a more energetically stable structure.

Supporting Information

Supporting Information is available from the Wiley Online Library or from the author.

Acknowledgements

K.W. and H.W. contributed equally to this work. The authors thank Zhenlu Zhang from Shenzhen University for the XRD Rietveld refinement analysis. P.Y. and M.S. thank the National Natural Science Fund for Innovative Research Groups (Grant No. 51621003), the National Key Research and Development Program of China (Grant No. 2016YFB0700700), and Beijing Municipal Found for Scientific Innovation (PXM2019_014204_500031). Z.L. thanks the National Natural Science Foundation of China (Grant No. 51802092). Computational resources from National Supercomputing Center in Changsha are gratefully acknowledged.

Conflict of Interest

The authors declare no conflict of interest.

Keywords

doping, layered cathodes, precipitation strengthening, TEM

Received: July 26, 2019
Revised: September 5, 2019
Published online: October 3, 2019

[1] Y. K. Sun, Z. Chen, H. J. Noh, D. J. Lee, H. G. Jung, Y. Ren, S. Wang, C. S. Yoon, S. T. Myung, K. Amine, *Nat. Mater.* **2012**, *11*, 942.
[2] M. Armand, J. M. Tarascon, *Nature* **2008**, *451*, 652.
[3] Y. Xiao, X. D. Zhang, Y. F. Zhu, P. F. Wang, Y. X. Yin, X. Yang, J. L. Shi, J. Liu, H. Li, X. D. Guo, B. H. Zhong, Y. G. Guo, *Adv. Sci.* **2019**, *6*, 1801908.
[4] N. Yabuuchi, K. Kubota, M. Dahbi, S. Komaba, *Chem. Rev.* **2014**, *114*, 11636.
[5] S. Guo, J. Yi, Y. Sun, H. Zhou, *Energy Environ. Sci.* **2016**, *9*, 2978.
[6] C. Wu, W. Hua, Z. Zhang, B. Zhong, Z. Yang, G. Feng, W. Xiang, Z. Wu, X. Guo, *Adv. Sci.* **2018**, *5*, 1800519.
[7] H. Kim, J. C. Kim, M. Bianchini, D.-H. Seo, J. Rodriguez-Garcia, G. Ceder, *Adv. Energy Mater.* **2018**, *8*, 1702384.
[8] Y.-H. Zhu, X. Yang, T. Sun, S. Wang, Y.-L. Zhao, J.-M. Yan, X.-B. Zhang, *Electrochem. Energy Rev.* **2018**, *1*, 548.
[9] M. D. Radin, J. Alvarado, Y. S. Meng, A. Van der Ven, *Nano Lett.* **2017**, *17*, 7789.
[10] C. Delmas, C. Fouassier, P. Hagenmuller, *Physica B+C* **1980**, *99*, 81.
[11] J.-N. Zhang, Q. Li, C. Ouyang, X. Yu, M. Ge, X. Huang, E. Hu, C. Ma, S. Li, R. Xiao, W. Yang, Y. Chu, Y. Liu, H. Yu, X.-Q. Yang, X. Huang, L. Chen, H. Li, *Nat. Energy* **2019**, *4*, 594.
[12] J. Kim, H. Lee, H. Cha, M. Yoon, M. Park, J. Cho, *Adv. Energy Mater.* **2018**, *8*, 1702028.
[13] G.-L. Xu, Q. Liu, K. K. S. Lau, Y. Liu, X. Liu, H. Gao, X. Zhou, M. Zhuang, Y. Ren, J. Li, M. Shao, M. Ouyang, F. Pan, Z. Chen, K. Amine, G. Chen, *Nat. Energy* **2019**, *4*, 484.
[14] C. Xu, W. Xiang, Z. Wu, Y. Xu, Y. Li, Y. Wang, Y. Xiao, X. Guo, B. Zhong, *ACS Appl. Mater. Interfaces* **2019**, *11*, 16629.
[15] L. Qiu, W. Xiang, W. Tian, C.-L. Xu, Y.-C. Li, Z.-G. Wu, T.-R. Chen, K. Jia, D. Wang, F.-R. He, X.-D. Guo, *Nano Energy* **2019**, *63*, 103818.
[16] J. Y. Hwang, S. T. Myung, Y. K. Sun, *Chem. Soc. Rev.* **2017**, *46*, 3529.
[17] Y. Xiao, P. F. Wang, Y. X. Yin, Y. F. Zhu, Y. B. Niu, X. D. Zhang, J. Zhang, X. Yu, X. D. Guo, B. H. Zhong, Y. G. Guo, *Adv. Mater.* **2018**, *30*, 1803765.
[18] W. Li, B. Song, A. Manthiram, *Chem. Soc. Rev.* **2017**, *46*, 3006.
[19] Y. You, A. Manthiram, *Adv. Energy Mater.* **2018**, *8*, 1701785.
[20] B. Xiao, X. Sun, *Adv. Energy Mater.* **2018**, *8*, 1802057.
[21] F. Lin, I. M. Markus, D. Nordlund, T. C. Weng, M. D. Asta, H. L. Xin, M. M. Doeff, *Nat. Commun.* **2014**, *5*, 3529.
[22] H. Kim, M. G. Kim, H. Y. Jeong, H. Nam, J. Cho, *Nano Lett.* **2015**, *15*, 2111.
[23] G. G. Amatucci, J. M. Tarascon, L. C. Klein, *Solid State Ionics* **1996**, *83*, 167.
[24] K. Xu, *Chem. Rev.* **2014**, *114*, 11503.
[25] K. Xu, *Chem. Rev.* **2004**, *104*, 4303.
[26] K. Wang, P. Yan, M. Sui, *Nano Energy* **2018**, *54*, 148.
[27] P. Yan, J. Zheng, T. Chen, L. Luo, Y. Jiang, K. Wang, M. Sui, J.-G. Zhang, S. Zhang, C. Wang, *Nat. Commun.* **2018**, *9*, 2437.
[28] P. Yan, J. Zheng, M. Gu, J. Xiao, J. G. Zhang, C. M. Wang, *Nat. Commun.* **2017**, *8*, 14101.
[29] R. Xu, L. S. de Vasconcelos, J. Shi, J. Li, K. Zhao, *Exp. Mech.* **2018**, *58*, 549.
[30] Z. Xu, M. M. Rahman, L. Mu, Y. Liu, F. Lin, *J. Mater. Chem. A* **2018**, *6*, 21859.
[31] J. Vetter, P. Novák, M. R. Wagner, C. Veit, K. C. Möller, J. O. Besenhard, M. Winter, M. Wohlfahrt-Mehrens, C. Vogler, A. Hammouche, *J. Power Sources* **2005**, *147*, 269.
[32] H.-H. Ryu, K.-J. Park, C. S. Yoon, Y.-K. Sun, *Chem. Mater.* **2018**, *30*, 1155.
[33] T. Joshi, K. Eom, G. Yushin, T. F. Fuller, *J. Electrochem. Soc.* **2014**, *161*, A1915.
[34] P. F. Wang, Y. You, Y. X. Yin, Y. S. Wang, L. J. Wan, L. Gu, Y. G. Guo, *Angew. Chem., Int. Ed.* **2016**, *55*, 7445.
[35] Q. Xie, W. Li, A. Manthiram, *Chem. Mater.* **2019**, *31*, 938.
[36] G. Singh, N. Tapia-Ruiz, J. M. Lopez del Amo, U. Maitra, J. W. Somerville, A. R. Armstrong, J. Martinez de Ilarduya, T. Rojo, P. G. Bruce, *Chem. Mater.* **2016**, *28*, 5087.

[37] X. Rong, E. Hu, Y. Lu, F. Meng, C. Zhao, X. Wang, Q. Zhang, X. Yu, L. Gu, Y.-S. Hu, H. Li, X. Huang, X.-Q. Yang, C. Delmas, L. Chen, *Joule* **2018**, *3*, 1.
[38] Q. Liu, X. Su, D. Lei, Y. Qin, J. Wen, F. Guo, Y. A. Wu, Y. Rong, R. Kou, X. Xiao, F. Aguesse, J. Bareño, Y. Ren, W. Lu, Y. Li, *Nat. Energy* **2018**, *3*, 936.
[39] Q. C. Wang, J. K. Meng, X. Y. Yue, Q. Q. Qiu, Y. Song, X. J. Wu, Z. W. Fu, Y. Y. Xia, Z. Shadike, J. Wu, X. Q. Yang, Y. N. Zhou, *J. Am. Chem. Soc.* **2019**, *141*, 840.
[40] K. Zhang, D. Kim, Z. Hu, M. Park, G. Noh, Y. Yang, J. Zhang, V. W. Lau, S. L. Chou, M. Cho, S. Y. Choi, Y. M. Kang, *Nat. Commun.* **2019**, *10*, 5203.
[41] J. Billaud, G. Singh, A. R. Armstrong, E. Gonzalo, V. Roddatis, M. Armand, T. Rojo, P. G. Bruce, *Energy Environ. Sci.* **2014**, *7*, 1387.
[42] B. Li, E. Ma, *Phys. Rev. Lett.* **2009**, *103*, 035503.
[43] A. Nie, Y. Cheng, Y. Zhu, H. Asayesh-Ardakani, R. Tao, F. Mashayek, Y. Han, U. Schwingenschlogl, R. F. Klie, S. Vaddiraju, R. Shahbazian-Yassar, *Nano Lett.* **2014**, *14*, 5301.
[44] Z. Liu, H. Deng, P. P. Mukherjee, *ACS Appl. Mater. Interfaces* **2015**, *7*, 4000.
[45] P. Yan, J. Zheng, Z.-K. Tang, A. Devaraj, G. Chen, K. Amine, J.-G. Zhang, L.-M. Liu, C. Wang, *Nat. Nanotechnol.* **2019**, *14*, 602.
[46] F. Izumi, K. Momma, *Solid State Phenom.* **2007**, *130*, 15.
[47] W. Kohn, L. J. Sham, *Phys. Rev.* **1965**, *140*, A1133.
[48] G. Kresse, D. Joubert, *Phys. Rev. B* **1999**, *59*, 1758.
[49] G. Kresse, J. Furthmüller, *Phys. Rev. B* **1996**, *54*, 11169.
[50] G. Henkelman, B. P. Uberuaga, H. Jonsson, *J. Chem. Phys.* **2000**, *113*, 9901.
[51] R. Xiao, H. Li, L. Chen, *Chem. Mater.* **2012**, *24*, 4242.